JOURNAL OF CATALYSIS **179,** 483–494 (1998)
ARTICLE NO. CA982202

Structure, Texture, Surface Acidity, and Catalytic Activity of $AlPO_4$–ZrO_2 (5–50 wt% ZrO_2) Catalysts Prepared by a Sol–Gel Procedure

Felipa M. Bautista,* Juan M. Campelo,*,[1] Angel Garcia,* Diego Luna,* Jose M. Marinas,* Antonio A. Romero,* Gerardo Colon,† Jose A. Navio,† and Manuel Macias†

*Departamento de Química Orgánica, Facultad de Ciencias, Universidad de Córdoba, Avenida S. Alberto Magno, s/n°, E-14004 Córdoba, Spain; and †Instituto de Ciencia de Materiales de Sevilla, Centro de Investigaciones Científicas "Isla de la Cartuja," Avenida Américo Vespucio, s/n°, E-41092 Sevilla, Spain

Received March 17, 1998; revised May 26, 1998; accepted June 5, 1998

A series of $AlPO_4$–ZrO_2 (APZr) systems with various zirconia loadings (5–50 wt%) were prepared by sol–gel deposition of zirconia onto $AlPO_4$ and characterized by TGA/DTA, XRD, DRIFT, laser-Raman spectroscopy, SEM–EDX, XPS, ^{27}Al and ^{31}P MAS NMR, and nitrogen adsorption. Surface acid characterization was carried out through pyridine chemisorption and cyclohexene skeletal isomerization reaction. Addition of ZrO_2 onto $AlPO_4$ prevented the formation of monoclinic zirconia and increased the temperature of crystallization into the tetragonal form, so that APZr systems were still amorphous after calcination at 1073 K. This higher thermal stability was responsible for its large surface area as well as pore volume in relation to pure components. SEM showed nonhomogeneous distribution in morphology, texture, and particle size. Also, EDX and XPS indicated that the surface concentration ratios were practically the same as the expected values of stoichiometric composition. Moreover, ^{27}Al and ^{31}P MAS NMR showed that the local structure of the $AlPO_4$ support did not change with zirconia. Good correlations were obtained between catalytic activities in cyclohexene skeletal isomerization and surface acid densities of $AlPO_4$–ZrO_2 systems (as determined by pyridine chemisorption at 373 and 573 K).

INTRODUCTION

$AlPO_4$ can be used as a catalyst and support. As a catalyst, $AlPO_4$ is known to be active in several chemical processes, such as dehydration, isomerization, alkylation, rearrangement, retroaldolization, condensation, and Diels–Alder cycloaddition (1–8). Moreover, $AlPO_4$ is also used as a support for polymerization, oxidation, hydrogenation, reductive cleavage, or hydration catalysts (1, 9–15). The acid–base properties of $AlPO_4$ play an important role in catalytic reactions. By modifying the acid–base properties of $AlPO_4$, its catalytic activity can be controlled. Modification of an aluminum starting salt, calcination at high temperatures, and addition of alkali, fluoride, and sulfate ions and a metal oxide (1, 5–13) bring about changes in the physicochemical properties and catalytic activity of $AlPO_4$. In the latter case, the performance of such catalysts is greatly dependent on the nature of the metal oxide (Al_2O_3, SiO_2, TiO_2, ZnO, V_2O_5, MoO_3, or WO_3), the $AlPO_4$/metal oxide ratio, the methods of preparation, and the operating conditions (1, 5–13).

On the other hand, the use of ZrO_2 as a catalyst or catalyst support has been steadily gaining importance due to such unique properties as its acidic, basic, and also oxidizing or reducing (redox) properties (16). The activity, selectivity, and stability of the zirconia catalyst are dependent on the method of preparation, the precursor, and the pretreatment (17, 18). However, crystallization and sintering of the crystals on calcination are detrimental to their use as a catalyst. Thus, control of the preparation method (19, 20) or the incorporation of different metals (21, 22) improves the thermal stability reflected as an increase in the crystallization temperature in the tetragonal phase. Also, incorporation of sulfur (23–26), leading to sulfated zirconia catalysts able to isomerize paraffins, under mild conditions (23, 26, 27), improves their thermal stability and hence their specific surface area. Moreover, sulfation of the zirconia in the amorphous rather than in the tetragonal or monoclinic state is highly preferred to obtain active catalysts (28). However, during calcination of amorphous sulfated zirconia, crystallization into a tetragonal phase occurs, and the active sample appears then to be a sulfated tetragonal zirconia. Good thermal stability is therefore necessary to avoid the tetragonal-to-monoclinic transition. The tetragonal phase has a higher content of nonbridging surface hydroxyl groups than the monoclinic phase, and this seems to be a crucial factor for producing active materials (23, 28, 29).

In the present work a series of $AlPO_4$–ZrO_2 catalysts, with zirconia loading in the range 5–50 wt%, were prepared by deposition of ZrO_2, following a sol–gel procedure, onto amorphous $AlPO_4$ catalyst thermally treated at 923 K. The materials were characterized by several physical methods [thermogravimetric analysis (TGA)/differential

[1] To whom correspondence should be addressed.

0021-9517/98 $25.00

thermal analysis (DTA), X-ray powder diffraction (XRD), laser-Raman (LRa) spectroscopy, scanning electron microscopy (SEM)–energy-dispersive X-rays (EDX), X-ray photoelectron spectroscopy (XPS), diffuse reflectance infrared spectroscopy (DRIFT), ^{27}Al and ^{31}P MAS NMR, and nitrogen adsorption–desorption (77 K)], with emphasis on crystallization, phase structure, surface area, pore volume, pore size distribution, and surface acid character. The goal of the present work was to prepare zirconia-based catalysts with a low degree of crystallinity and/or thermally stable tetragonal phase.

EXPERIMENTAL

Materials

A synthetic amorphous $AlPO_4$ catalyst was used as zirconia carrier. Synthetic $AlPO_4$ was obtained by precipitation with ethylene oxide from aqueous solutions of $AlCl_3 \cdot 6H_2O$ and H_3PO_4 (85 wt%) as described elsewhere (30). The solid thus obtained was washed with 2-propanol, dried at 393 K for 24 h, and then calcined at 923 K for 3 h.

Zirconia was deposited onto $AlPO_4$ carrier by a sol–gel chemical route using $ZrOCl_2 \cdot 8H_2O$ (Fluka, 43–44% ZrO_2) as precursor. The precise preparation method for an APZr system with 10 wt% ZrO_2 (APZr-10) was as follows: an aqueous solution on zirconium oxychloride (0.9 M) was slowly added, under vigorous stirring, into a suspension of $AlPO_4$ (10 g, dried at 383 K for 48 h) in 200 cm^3 of a buffered phosphate solution (pH 7) standardized against NBS, pH 6.86 (KH_2PO_4/Na_2HPO_4), to prevent dissolution of $AlPO_4$. After mixing both, the resulting suspension was maintained with continuous stirring at room temperature for 24 h and, then, a hydrogel was obtained. During this aging step, the pH was controlled. The gel was filtered and washed repeatedly with doubly distilled water until no chloride anion signal was detected in filtering water ($AgNO_3$ test). Afterward, the precipitated gel was dried at room temperature for 24 h, then in an oven at 383 K for 24 h, and, finally, calcined at 873, 1073, or 1273 K for 3 h in a muffle furnace. Samples thus prepared were labeled APZr followed by two hyphenated, separate numbers that indicated, respectively, the zirconia loading (wt%) and the calcination temperature (APZr-5-873, APZr-35-1273, and so on). The processing route of the $AlPO_4$–ZrO_2 (APZr, 5–50 wt% ZrO_2) samples is shown in detail in Scheme 1.

A portion of the $AlPO_4$ was similarly treated, dried, and calcined but in the absence of zirconia precursor compound so as to serve as blank materials. These were denoted as AP-0 followed by the calcination temperature (AP-0-873 and so on).

Pure zirconia was also obtained by the same sol–gel procedure, in 200 cm^3 of a buffered phosphate solution (pH 7), to serve as blank materials. These were denoted as ZrO_2 followed by the calcination temperature (ZrO_2-873, ZrO_2-1073 and ZrO_2-1273).

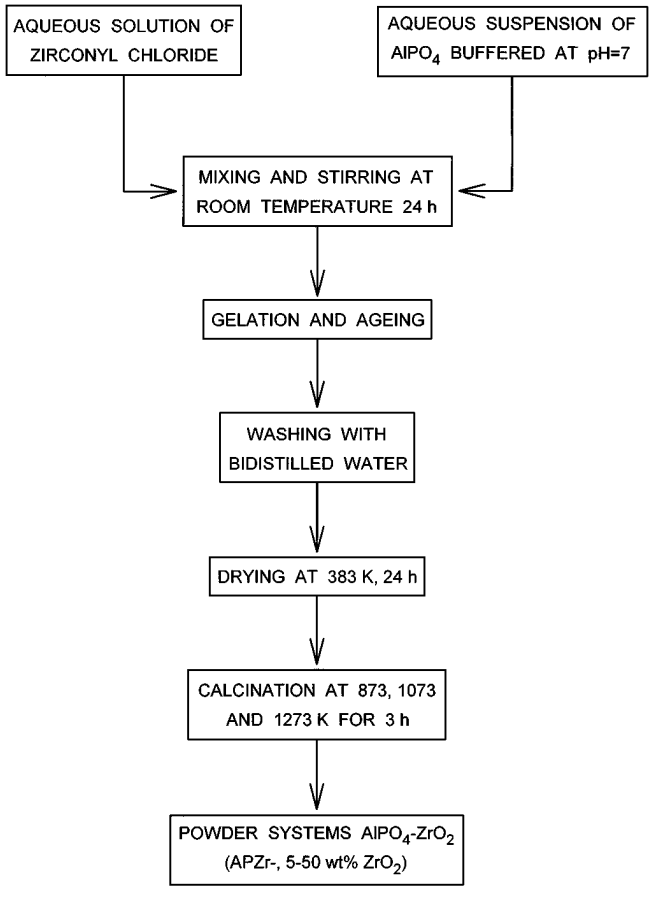

SCHEME 1

On the other hand, on the thermally treated samples we did not detect (XPS and EDX, analysis, see below) either alkaline cations (Na^+, K^+, etc.) or chloride anions, evidence of practical elimination of such ions fron our catalysts after the pretreatment.

Thermogravimetry and Differential Thermal Analysis

Thermogravimetric and differential thermal analyses (DTA) were performed simultaneously using a high-temperature thermal analyzer (Setaram 92, Model 16.18) in the presence of static air at a heating rate of 10 K min^{-1} (temperature range: 273–1473 K). Finely powdered α-alumina was used as a reference material. The sample used was the dried zirconia-impregnated $AlPO_4$ support (393 K, 24 h) prior to calcination.

XRD Measurements

X-ray powder diffractometry was carried out at 300 K and in the 2θ range between 10° and 80° (at a scanning speed of 2° min^{-1}) using a Siemens D5000 diffractometer equipped with Ni-filtered Cu$K\alpha$ radiation ($\lambda = 1.5405$ Å) at 35 kV and 20 mA. The crystalline bulk structures of the

materials were elucidated by matching the XRD patterns observed with JCPDS standards. This pattern matching was carried out automatically by means of an on-line library search system (PFD Data Base).

Laser-Raman Spectroscopy Measurements

Laser-Raman spectra were taken from lightly compacted samples at 3600–200 cm^{-1} and a resolution of 0.2 cm^{-1}, using a Perkin–Elmer System 2000 Fourier-transform (FT) Raman spectrometer equipped with a near-infrared diode-pumped Nd: YAG laser (1.064 μm). The laser powder at the sample was in the range 5–100 mW.

NMR Spectroscopy

^{27}Al (pulse: 0.6 μs; recycle delay: 0.3 s) and ^{31}P (pulse: 2.6 μs; recycle delay: 6 s) MAS NMR spectra were recorded at resonance frequencies ν_0 of 104.26 and 128.38 MHz, respectively, with a Bruker ACP-400 multinuclear spectrometer (external magnetic field of 9.4 T).

NMR measurements were carried out on samples previously dried at 413 K for at least 96 h. Immediately after they had been dried, the samples were rapidly transferred to spinners to keep hydration effects to a minimum. Measurements were carried out at room temperature with a standard Bruker double-bearing MAS (5.6 kHz) probe. About 200 mg of sample material was placed in the zirconium dioxide rotor (4 mm) with a volume of about 0.35 cm^3. The references for ^{27}Al and ^{31}P were $Al(H_2O)_6^{3+}$ and 85% H_3PO_4, respectively.

To preserve quantitative analysis, no mathematical procedures of NMR signal treatment, such as multiplication by an exponential function, were used. Also, the chemical shifts given for aluminum was not corrected for second-order quadrupole effects.

Scanning Electron Microscopy

SEM studies were carried out in a Jeol apparatus (Model JSM-5400) and the dispersion energy of X-rays was measured with a Link Isis Pentafet Model analyzer; a semiautomatic image analyzer of magnetostrictive Kontron MOP-30 board was used to estimate the average weight size of aggregates and particles. Selected scanning electron micrographs of many visual fields studied were reported here.

XPS Measurements

The X-ray photoelectron spectra were recorded in a Leybold–Heraeus LHS-10 spectrometer working with a pass energy constant of 50 eV and using Al$K\alpha$ radiation ($h\upsilon = 1686.6$ eV) as the excitation source. The spectra were submitted to background subtraction and to area calculations. Binding energy values were referred to as C(1*s*) peak (pollution carbon) at 284.6 eV. A final pressure of 10^{-9} Torr was always attained before XPS recording.

DRIFT Measurements

DRIFT spectra were recorded in a FTIR instrument (Bomen MB-100) equipped with an "environmental chamber" (Spectra Tech, P/N 0030-100) placed in a diffuse reflectance attachment (Spectra Tech, Collector). A resolution of 8 cm^{-1} was used with 256 scans averaged to obtain a spectrum from 4000 to 400 cm^{-1}. Single-beam spectra were ratioed against KBr collected at the same temperature as the sample. A plot of pseudoabsorbance was preferred. The temperature controller was calibrated to the actual temperature by inserting a thermocouple directly into the sample and monitoring the sample temperature at different controller settings. The samples were diluted to 15% in KBr.

DRIFT spectra were recorded for all the calcined (873 K) catalysts previously dried at 400 K for 24 h under vacuum. Afterward, the catalyst was placed in the environmental chamber cell with a 20 cm^3 min^{-1} flow of dehydrated and deoxygenated nitrogen, heated to 573 K, and held at this temperature for 1 h prior to recording the spectrum. Longer nitrogen flushing times or vacuum treatment do not modify the DRIFT spectra. In some cases, spectra of the O–H stretching region were smoothed with a five-point Savitzky–Golay algorithm.

Surface Area and Pore Properties

Surface-area and pore-size information was obtained from nitrogen adsorption–desorption isotherms at 77 K, using a Micromeritics ASAP 2000 analyzer. Prior to measurements, all samples were degassed to 0.1 Pa. BET surface areas were calculated assuming a cross-sectional area of 0.162 nm^2 for the nitrogen molecule. Assessments of possible microporosity were made from *t*-plot constructions, using the Harkins–Jura correlation for t as a function of p/p_0. Parameters were fitted to a low-area, nonporous silica. Mesopore size distributions were calculated using the Barret–Joyner–Halenda (BJH) method (31), using the Halsey equation (32) and assuming a cylindrical pore model.

Surface Acid Properties

The surface acidity was measured in a dynamic mode by means of the gas-phase adsorption of pyridine (PY) at 373 and 573 K, using a pulse chromatographic technique (33). The pulse size was in the range of gas chromatography linearity, corresponding to 0.1–0.5 monolayer. The acidity measurements were repeated several times and good reproducibility of the results was obtained (ca. 7%).

Catalytic Measurements

Cyclohexene conversion was carried out in a microcatalytic pulse reactor according to a method previously described (6). Initially a series of pulses of varying size were injected onto the catalyst to optimize the pulse size within

the linear range of the adsorption isotherm. Thus, catalytic measurements were performed under the following conditions: cyclohexene (liquid) volume/pulse size: 1 μl; catalyst weight: 20–70 mg; temperature: 523–673 K (25 K intervals); flow rate of nitrogen (99.999%, $H_2O < 3$ ppm, Air Liquide Spain) carrier: 40 $cm^3\ min^{-1}$; GC with FID and two columns ($\frac{1}{8}$ in., stainless steel, 2 m each) in series packed with, respectively, 5% polyphenyl ether (six rings) and 5% squalene on Chromosorb G AW-DMCS 80/100 at 323 K. A fresh catalyst was used on each run, and before each run, the catalyst was pretreated *in situ* heating under nitrogen (40 $cm^3\ min^{-1}$) for 1 h at 573 K. A blank test showed that there was insignificant thermal reactivity in the absence of the catalyst.

The reaction products, characterized by GC-MS (HP 5970 MSD quadrupole mass spectrometer) were 1- and 3-methylcyclopentene (1- and 3-MCPE).

Cyclohexene (from Aldrich) was used after distillation and purification with a column of alumina previously calcined at 573 K for 3 h.

RESULTS AND DISCUSSION

TGA/DTA Measurements

The DTA profile for the APZr-35 sample is shown in Fig. 1. The remaining APZr samples displayed almost the same behavior. The TGA profile was characterized by weight loss up to 823 K. Below 823 K the weight loss (which was accompanied by an endothermic band at 425 K in the DTA profile) can be attributed to the desorption of weakly adsorbed water. Between 823 and 1473 K, a slight weight loss is observed, due mainly to the condensation of surface hydroxyls, together with two exothermic DTA peaks (without a corresponding TGA peak). The first exothermic transition (1206 K) corresponded to crystallization of the amorphous ZrO_2 into the ZrO_2 tetragonal phase (see XRD results below). The position of this band depended on the zirconia loading of the APZr system. Thus, as zirconia loading increased, the exothermic peak shifted to slightly lower temperatures. The second exothermic transition (1344 K) corresponded to crystallization of the amorphous $AlPO_4$ into the $AlPO_4$- tridymite form (see XRD results below). The position of this band also depended on the zirconia loading of the APZr system and, thus, as zirconia loading increased, the exothermic peak shifted to higher temperatures (in the absence of zirconia, $AlPO_4$ crystallized in the tridymite form at 1055 K).

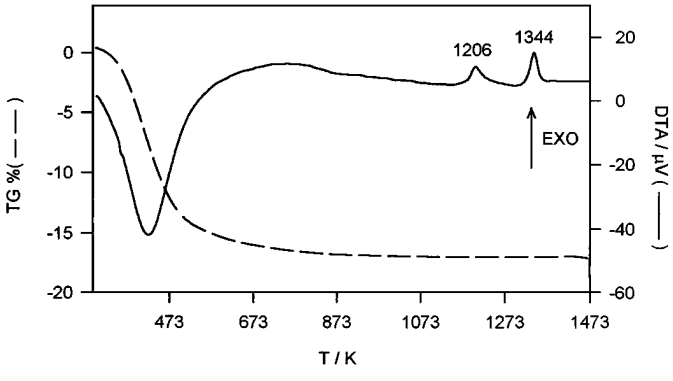

FIG. 1. DTA curve for APZr-35 sample. Static air atmosphere; 10 K min^{-1} scan.

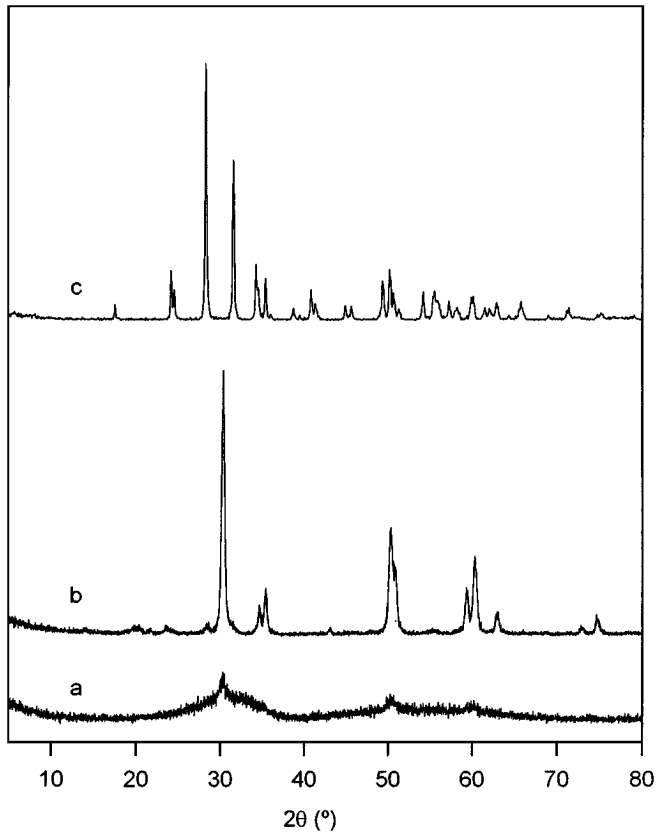

FIG. 2. Powder XRD profiles (Cu$K\alpha$, $\lambda = 1.5405$ Å) of zirconia samples: (a) amorphous zirconia, ZrO_2-873; (b) tetragonal zirconia, ZrO_2-1273; (c) commercial monoclinic zirconia (ceramic grade, Aldrich).

So, the presence of ZrO_2 delayed the transformation of the amorphous $AlPO_4$ into the tridymite $AlPO_4$. Likewise, the presence of $AlPO_4$ also delayed the crystallization of zirconia into the tetragonal modification.

XRD Measurements

ZrO_2 materials. Zirconium oxide had three well-defined polymorphs: the monoclinic baddeleyite phase, which is stable to about 1373 K; the tetragonal phase, which appeared during annealing treatment up to 1473 K; and the cubic phase, which the compounds adopted at about 2643 K (34). In addition, amorphous ZrO_2 was frequently observed when it was prepared by sol–gel processes (35). In our case, the powder X-ray diffraction patterns of zirconia samples obtained in phosphate-buffered solution and calcined in the range 873–1273 K are presented in Fig. 2. This showed that

the ZrO_2-873 sample has a very low degree of crystallinity as revealed by the broad band centered at approximately $2\theta = 30^\circ$ (Fig. 2a). Moreover, ZrO_2 samples calcined at 1073 and 1273 K (Fig. 2b) showed the characteristic peaks of the well-crystallized tetragonal phase, as revealed by its intense [111] line at $2\theta = 30^\circ$. It is interesting to note that the characteristic peaks corresponding to the monoclinic phase [lines at $d = 3.16$ Å ($2\theta = 28.2^\circ$), $d = 2.83$ Å ($2\theta = 31.6^\circ$), and $d = 2.62$ Å ($2\theta = 34.2^\circ$)] were suppressed (Fig. 2c) when zirconia was obtained in phosphate-buffered solution (pH 7).

Thus, when zirconia samples are obtained by precipitation of the gel, but in the absence of a phosphate-buffered solution (pH 7), the crystallization process takes place at around 623 K (36). The predominant phase is the tetragonal one with slight participation of the monoclinic phase. This later phase developed with calcination temperature, becoming predominant for calcination temperatures higher than 873 K (monoclinic molar fraction: 0.95). So, the tetragonal phase was predominant only over a limited range of temperatures (between 573 and 723 K).

Our results indicated that the presence of a phosphate-buffered solution (pH 7) stabilized the tetragonal phase, even at 1273 K. The hindrance in the crystallization of the ZrO_2 samples obtained in phosphate-buffered solution was probably due to the presence of PO_4^{3-} species on the surface, as occurred on other ZrO_2 samples modified by phosphoric acid impregnation (37, 38). In this sense, oxides of hexavalent ions, such as WO_3, MoO_3, and other transition metal oxides, were reported to delay the crystallization of zirconia and to stabilize the tetragonal structure (39). Formation of metastable tetragonal zirconia was attributed to the structural similarity between an amorphous and the tetragonal structure in which the interatomic distances Zr–O and Zr–Zr were similar (40, 41). Thus, a small deformation of the short-range structure was required for the crystallization to the tetragonal modification. Parallel to the crystallographic changes reported above, there are textural modifications (see below). However, the most striking feature of the present results was that zirconia remained amorphous even at calcination temperatures of 873 K.

$AlPO_4$–ZrO_2 (5–50 wt% ZrO_2) materials. All APZr samples calcined at 873 and 1073 K (except APZr-5-1073) have a very low degree of crystallinity as revealed in Fig. 3, where, as an example, appear the X-ray diffraction patterns of the APZr-35 sample thermally treated at different temperatures. Thus, from Fig. 3a, it can be seen that thermal treatment at 1151 K resulted in only two very broad bands in the 2θ ranges 20° to 40° and 40° to 65°, indicating that the derived APZr-35 sample has a very low degree of crystallinity. From Fig. 3b, it can be seen that the thermal treatment at a higher temperature (1263 K) developed bands corresponding to the ZrO_2 tetragonal phase. Thermal treatment at 1473 K (after DTA measurements) did not alter the ZrO_2 XRD pattern phase of the sample, although the peaks

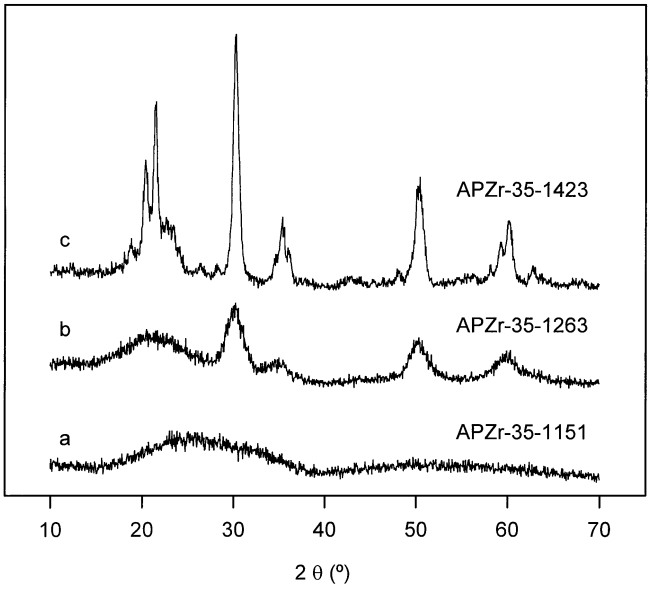

FIG. 3. Powder XRD profiles (Cu$K\alpha$, $\lambda = 1.5405$ Å) of APZr-35 sample thermally treated at increasing temperatures.

became sharper and stronger, indicating that ZrO_2 was well crystallized in the tetragonal phase (Fig. 3c). In addition, $AlPO_4$ crystallized in the tridymite form. The transition of the tetragonal ZrO_2 into the monoclinic phase did not take place.

Moreover, the thermal behavior of the APZr-5 sample was parallel to that of the AP-0 sample. Thus, even at 1273 K, $AlPO_4$ crystallized in the tridymite form. Therefore, taking into account that the crystallization temperature of $AlPO_4$ in APZr gels showed a general tendency to increase with ZrO_2 content, the presence of ZrO_2, in an amount higher than 5 wt%, delayed the transformation of the amorphous $AlPO_4$ into the tridymite $AlPO_4$, which reflected the higher thermal stability of APZr gels. Likewise, the presence of $AlPO_4$ also delayed the crystallization of zirconia into the tetragonal modification. Accordingly, APZr materials were still amorphous after calcination at 1073 K unlike pure components. Also, formation of the tetragonal modification appeared at 1273 K and was complete at 1423–1473 K without any monoclinic zirconia being formed at the same time.

Laser-Raman Analysis

Figure 4 shows the Raman spectra of some representative ZrO_2 and APZr samples. The spectrum of ZrO_2-1273 (Fig. 4b) reveals six bands at 190, 270, 315, 455, 602, and 645 cm^{-1}. Ishigame and Sakurai (42) measured the Raman spectra of the ZrO_2 tetragonal phase at a high temperature and also found six bands (at 190, 270, 315, 456, 610, and 645 cm^{-1}), as predicted by the group theory. Thus, the bands observed in Fig. 4b were assigned to the tetragonal ZrO_2 phase (space group $P4_2/nmc$) (43, 44) and their

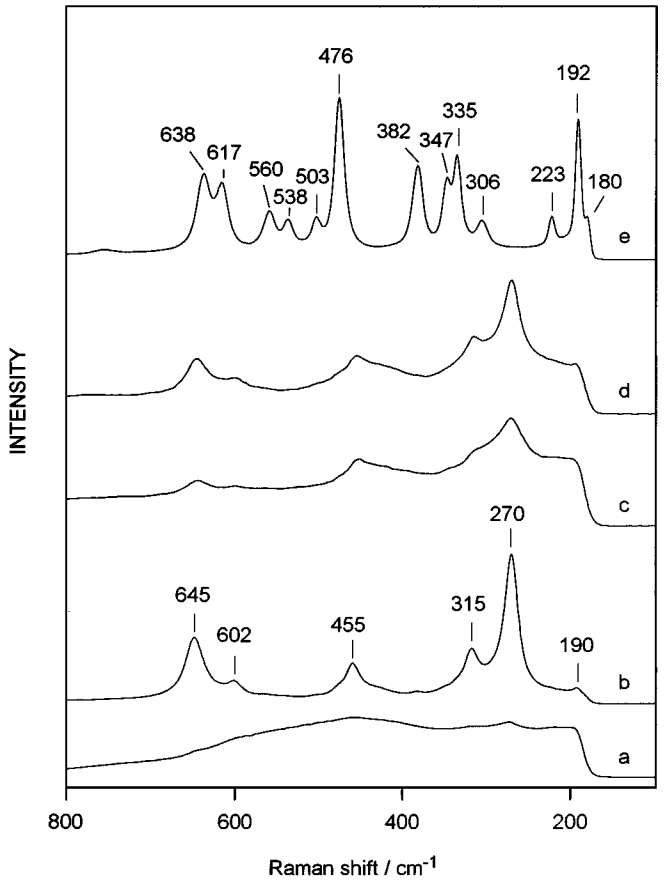

FIG. 4. Typical laser-Raman spectra of different ZrO_2 and $AlPO_4$–ZrO_2 samples: (a) amorphous zirconia, ZrO_2-873; (b) tetragonal zirconia, ZrO_2-1273; (c) APZr-35-1273; (d) APZr-50-1273; (e) commercial monoclinic zirconia (ceramic grade, Aldrich).

average size was in fair agreement with the Raman spectra of ZrO_2 tetragonal single crystals (45) and of a stabilized crystalline sample of ZrO_2 containing 4.6 mol% Y_2O_3 (46).

With respect to APZr samples, laser-Raman spectroscopy detected some bands only when the thermal treatment reached 1273 K. These bands corresponded to the ZrO_2 tetragonal phase (Figs. 4c, 4d). In addition, as expected, the bands increased in intensity with the ZrO_2 content of the APZr sample. In no case, even after DTA measurements (1423–1473 K), did laser-Raman spectroscopy detect the presence of monoclinic ZrO_2, characterized by bands at 180, 192, 223, 306, 335, 347, 382, 476, 503, 538, 560, 617, and 638 cm^{-1} with the main feature at 476 cm^{-1} (35, 42, 44, 46), as can be seen in Fig. 4e, where the Raman spectra of commercial monoclinic ZrO_2 (Aldrich, ceramic grade) are shown. These results are in line with those reported above concerning XRD analysis.

^{27}Al and ^{31}P MAS NMR Spectroscopy

The ^{27}Al MAS NMR spectra (not shown) of $AlPO_4$ and $AlPO_4$–ZrO_2 (5–50 wt% ZrO_2) exhibited a broad peak at around 39 ppm, typical of tetrahedral aluminum with phosphorus in the second coordination sphere, i.e., sharing oxygens with four tetrahedra of phosphorus [$Al(OP)_4$] (47, 48). The strong upfield shift observed with respect to other aluminum oxides was attributed by Muller *et al.* (47) to the influence of P atoms located in the second coordination sphere of Al. Moreover, the ^{31}P MAS spectra (not shown) also exhibited one single broad component whose isotropic chemical shift value appeared at around −26 ppm. This chemical shift corresponded to P atoms in tetrahedral coordination with P–O–Al bonds [i.e., $P(OAl)_4$ environments]. In addition, it appears that the chemical shifts of P at different sites were similar, resulting in a broadened peak. Furthermore, the incorporation of zirconia did not change the isotropic chemical shift value of the ^{27}Al and ^{31}P peaks so that the local structure of the $AlPO_4$ support was not changed by zirconia.

XPS Measurements

Table 1 summarizes the information about the elemental surface composition and XPS binding energies (in parentheses) of the elements present on the surface of APZr samples. As can be seen from Table 1, the surface concentration ratio $[P]_s/[Al]_s$ of APZr systems varies from 1 to 1.5. Since the P/Al ratio of the blank reference sample AP-0-873 is 0.88 and our results show that the surface concentration ratio P/Al of APZr systems varies from 1 to 1.5, one other possible explanation of the excess of phosphate ions is to assume that this excess could come from the phosphate-buffered solution. At the same time, a simple calculation of the [Zr]/[Al] ratios indicates that the surface concentration ratio $[Zr]_s/[Al]_s$ is greater than the ratios corresponding to the expected theoretical stoichiometric composition. Moreover, the ratios of oxygen to cations (Al + P + Zr) for the APZr samples slightly exceeded the expected value of stoichiometric composition ([O]/[cations] = 2) and seemed to increase as the zirconia content increased. This may be due to the presence of hydroxyl groups linked to the surface cations. This fact could be interpreted as the incorporation

TABLE 1

Elemental Surface Composition and XPS Binding Energies[a] of the Elements Present on the Surface of APZr Systems Calcined at 873 K for 3 h

System	Surface concentration (at.%)			
	P (2*p*)	Al (2*p*)	Zr (3*d*)	O (1*s*)
AP-0-873	14.4(133.5)	16.3(74.1)	—	67.1(531.5)
APZr-5-873	14.6(133.3)	14.6(74.1)	1.8(182.0)	65.5(531.5)
APZr-10-873	15.2(133.3)	12.5(74.1)	2.8(182.2)	66.5(531.3)
APZr-25-873	13.2(133.2)	12.4(74.1)	3.4(182.2)	67.1(531.2)
APZr-50-873	10.8(134.6)	7.2(75.2)	9.4(183.6)	65.3(532.4)

[a] In parentheses, eV.

of zirconia content on the $AlPO_4$ matrix leading to a modification of the surface Brønsted acidity by an effect on the degree of surface hydroxylation.

Furthermore, the various core lines investigated for different samples were very similar and they all appeared as single symmetrical lines indicating a homogeneous distribution of the electron densities around the atoms throughout the solid. Table 1 also lists the XPS binding energies of elements present on the surface. As indicated before, all values are referenced to the C(1*s*) peak.

SEM–EDX Studies

SEM revealed a very nonhomogeneous distribution in morphology and particle size for all APZr samples. In addition, no changes were observed either in morphology or in particle size when the amount of zirconia increased. A selected micrograph of an APZr sample is shown in Fig. 5a. The average size of the larger particles was around 50 μm, although in all samples a great population of very fine particles was observed. At the same time it should be mentioned that treatment of $AlPO_4$ with the buffer solution certainly produced a modification in the surface texture as shown in Figs. 5b and 5c, where it can be observed that the surface of $AlPO_4$ treated at pH 7 (Fig. 5c) was smoother than the nontreated one (Fig. 5b).

On the other hand, it was observed that all samples had particles with a thin and smooth external surface containing small deposits covering an internal sponge-like structure; this last observation is shown in Fig. 5d. Microanalysis (EDX) of the surface of the particles revealed a nonhomogeneous distribution of zirconium not only in the particles but also between the particles, probably associated with the preparation procedure. However, the acquisition of a general micrograph field showed values for the atomic percentage of zirconium similar to those obtained by XPS.

DRIFT Measurements

Several series of DRIFT experiments were completed to understand the effects of zirconia on the $AlPO_4$ support. The influence of zirconia on the support was studied by examining the hydroxyl and skeletal regions. The spectrum of pure amorphous $AlPO_4$, recorded after thermal

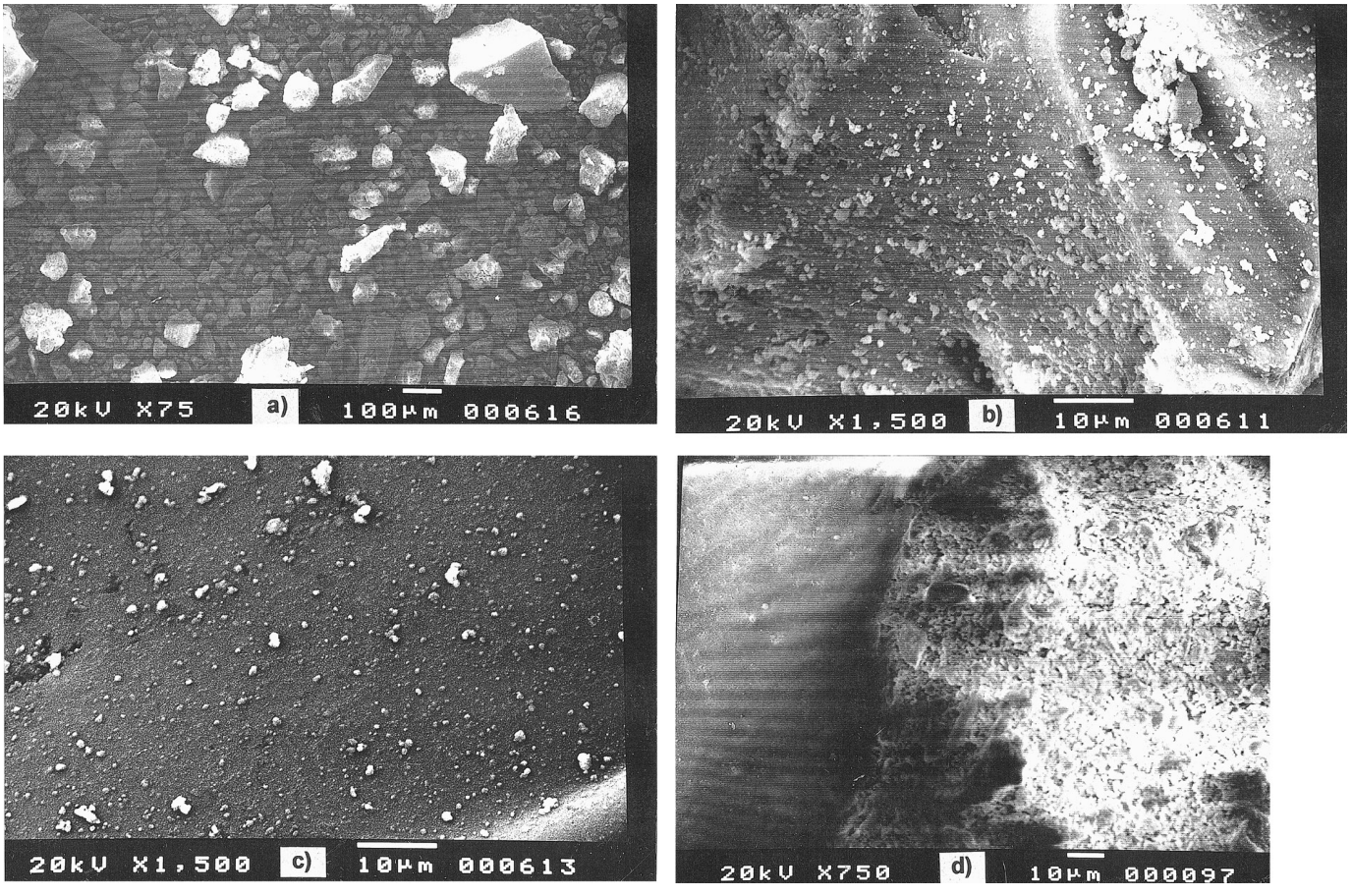

FIG. 5. Scanning electron micrographs of the surface particles: (a) APZr-10-873; (b) original $AlPO_4$ sample; (c) $AlPO_4$ buffered treated (AP-0-873); (d) a detail of a APZr-50-873 particle showing the differences in texture between the external smooth surface and the spongy internal part.

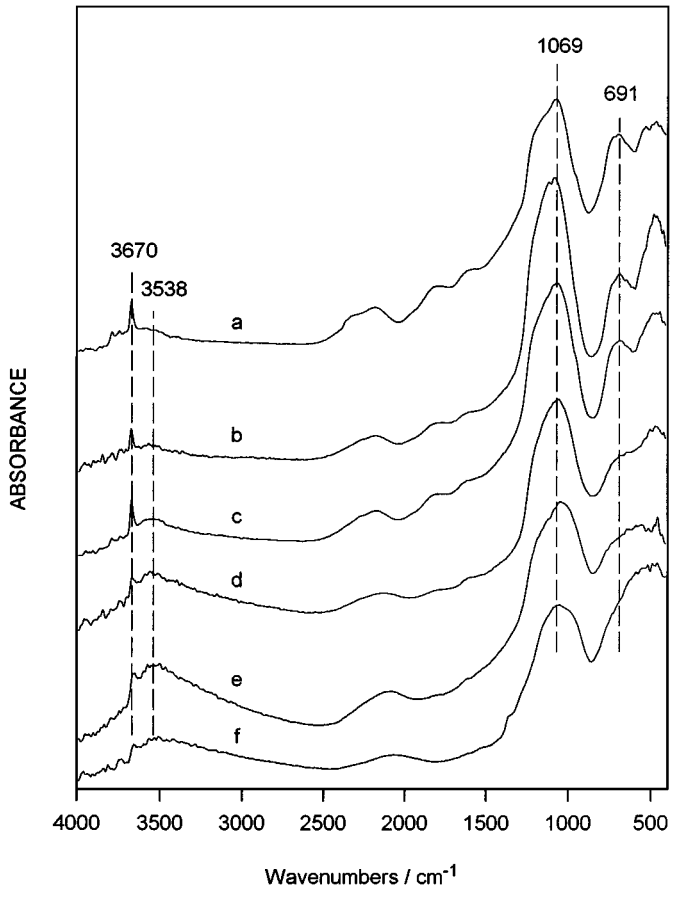

FIG. 6. DRIFT spectra of $AlPO_4$, ZrO_2, and $AlPO_4$-ZrO_2 samples recorded at 573 K in the nitrogen stream. (a) AP-0-873; (b) APZr-7-873; (c) APZr-10-873; (d) APZr-35-873; (e) APZr-50-873; (f) ZrO_2-873. All spectra were displaced for presentation.

pretreatment at 573 K for 1 h under a nitrogen flow (10 cm^3 min^{-1}), is shown in Fig. 6a. In the OH stretching vibration region (4000–2500 cm^{-1}) two isolated hydroxyl peaks were found, a weak one at 3786 cm^{-1} and a strong one at 3670 cm^{-1}, which were due to aluminum (with aluminum atoms in tetrahedral coordination) and phosphorus surface hydroxyl groups, respectively (1). Also a very broad band around 3538 cm^{-1} was found. This band is due to surface hydroxyl groups, most likely phosphorus ones, perturbed by a hydrogen bridge bond from a surface hydroxyl band.

The DRIFT spectra of the hydroxyl region of some APZr samples are shown in Figs. 6b to 6e. The incorporation of zirconia results in the gradual disappearance of Al–OH and P–OH bands. Likewise, the band around 3538 cm^{-1} becomes broader as in amorphous zirconia (Fig. 6f), indicating a larger number of hydrogen-bonded hydroxyl groups, most probably between P–OH and Zr–OH groups. However, some of the isolated P–OH groups were still present at 50 wt% ZrO_2.

The DRIFT spectra of the skeletal region (below 1700 cm^{-1}) showed that in the prepared APZr systems, the phosphorus atom remains as in the $AlPO_4$ support and, thus, it is surrounded by tetrahedra of oxygen atoms: bands due to triply degenerate P–O stretching vibration (~1069 cm^{-1}) ν_3 mode of tetrahedral PO_4^{3-}, triply degenerate O–P–O bending vibration (~480 cm^{-1}) ν_4 mode of PO_4^{3-} tetrahedra, and stretching vibration of Al–O bonds in combination with P–O bonds (~691 cm^{-1}). DRIFT data were in accordance with the XRD and ^{27}Al and ^{31}P MAS NMR data.

Surface Area and Pore Properties

The adsorption–desorption isotherms (not shown) of $AlPO_4$, ZrO_2, and $AlPO_4$–ZrO_2 (5–50 wt% ZrO_2) were of nearly the same type. From the shape of the curves it can be assumed that samples calcined up to 1073 K consist mainly of mesopores, showing isotherms as type IV in the BDDT classification (49) and hysteresis loops of *H1* type according to the classification proposed by IUPAC (50). The absence of microporosity, suggested by the shape of the isotherms, was confirmed using the Harkins–Jura correlation (51). Plots of multilayer thickness t versus volume of adsorbed nitrogen (V_p) could be extrapolated through the origin. Moreover, after calcination at 1273 K, the adsorption–desorption isotherms were invariably of type II, showing the nonporous nature of the samples.

The porous texture of the APZr samples was analyzed following the BJH method and assuming a cylindrical pore model (31). The analysis was applied to the adsorption branch of each isotherm, which is preferred to the desorption branch for type IV isotherms (52, 53). The cumulative surface area and pore volume were comparable to the corresponding measured values of S_{BET} and V_p. This agreement indicates the correct choice of the pore analysis method. The observed increasing slope of this t plot in the high-t region also supports the above assignment of pore shape (52).

The BET surface area (S_{BET}), pore volume (V_P, $p/p_0 =$ 0.99), main pore radius (r_P, $r_P = 2V_P/S_{BET}$), and pore volume distribution of $AlPO_4$, ZrO_2, and $AlPO_4$–ZrO_2 (5–50 wt% ZrO_2) are listed in Table 2.

As shown in Table 2, strong differences were apparent in the textural parameters of APZr catalysts depending on the zirconia loading and thermal treatment. Thus, the $AlPO_4$-treated support (AP-0) lost its surface area when calcining at 1073 K. Again, the behavior of the APZr-5 sample paralleled that of AP-0. However, zirconia loadings above 5 wt% stabilized surface area for calcination temperatures lower than 1273 K. Moreover, surface area increased when zirconia loading reached 25–35 wt%. Notwithstanding, the decrease in progressive surface area versus calcination temperature became smaller as the zirconia content of the catalyst increased up to 25 wt% and thereafter showed a strong decreasing trend, thus resembling those of pure zirconia.

TABLE 2

Textural Properties of $AlPO_4$, ZrO_2, and $AlPO_4$–ZrO_2 (5–50 wt% ZrO_2) Systems

Catalyst	S_{BET} (m^2/g)	V_p (cm^3/g)	r_p (nm)	Pore volume distribution (% vol)				
				>20 nm	10–20 nm	5–10 nm	2–5 nm	<2 nm
AP-0-873	154	0.46	6.0	28.7	36.5	27.4	6.8	0.6
AP-0-1073	1	—	—	—	—	—	—	—
APZr-5-873	119	0.49	8.2	48.4	30.9	16.2	4.1	0.5
APZr-5-1073	4	—	—	—	—	—	—	—
APZr-7-873	114	0.58	10.2	61.9	25.5	10.0	2.4	0.2
APZr-7-1073	103	0.54	10.6	65.4	24.9	7.4	1.9	0.3
APZr-7-1273	10	0.11	21.9	92.1	2.9	1.4	3.6	—
APZr-10-873	101	0.61	12.2	75.3	17.3	5.6	1.6	0.3
APZr-10-1073	94	0.58	12.3	76.4	15.6	6.0	1.7	0.3
APZr-10-1273	25	0.20	15.9	88.4	7.7	2.0	1.6	0.3
APZr-25-873	190	0.41	4.3	14.0	27.9	38.6	18.5	0.9
APZr-25-1073	165	0.38	4.6	16.9	29.6	35.7	17.0	0.8
APZr-25-1273	10	0.06	10.9	62.3	29.3	7.4	1.1	0.1
APZr-35-873	186	0.15	1.6	5.1	2.8	14.0	67.8	10.2
APZr-35-1073	103	0.09	1.7	8.3	3.4	18.9	69.5	—
APZr-35-1273	2	—	—	—	—	—	—	—
APZr-50-873	79	0.06	1.4	16.6	2.7	6.0	56.8	17.9
APZr-50-1073	13	0.01	2.2	42.2	4.2	7.5	46.1	—
APZr-50-1273	2	—	—	—	—	—	—	—
ZrO_2-873	104	0.08	1.5	8.3	2.7	9.6	65.3	14.1
ZrO_2-1073	13	0.02	3.6	27.8	7.5	22.7	42.0	—
ZrO_2-1273	1	—	—	—	—	—	—	—

These results can be accounted for by the fact that $AlPO_4$ crystallization showed a general tendency to increase with zirconia content, as shown by DTA and XRD measurements (see above).

On the other hand, pore volume increased with zirconia up to 10 wt% ZrO_2 and then decreased, especially above 25 wt% ZrO_2. Moreover, the decrease in progressive pore volume as zirconia loading and/or calcination temperature increased followed the same trend as the surface area. Also, the pore size distribution was displaced toward larger pores when zirconia loading increased up to a value of 10 wt%. Above this amount, the pore size distribution was displaced toward smaller pores so that APZr-35 and APZr-50 samples exhibited almost the same pore size distribution as zirconia.

The most striking feature of the results shown in Table 2, however, is that the presence of zirconia strongly influenced the development of textural properties with temperature when compared with $AlPO_4$. The protective effect of the addition of ZrO_2 to the surface area of the APZr systems, heated in air at different temperatures, was evident, especially at zirconia loadings in the range 7–25 wt% and at a calcination temperature of 1073 K.

These facts are important because the modification of the surface texture of $AlPO_4$ by ZrO_2 was accompanied by a rise in surface acidity and hence in catalytic activity for cyclohexene skeletal isomerization (see below).

Surface Acidity Measurements

The surface acidity of APZr catalysts (5–25 wt% ZrO_2) is given in Table 3 as the amount of pyridine chemisorbed at saturation at the given temperature. As expected, the surface chemical interaction in all APZr catalysts was determined by the adsorption temperature. As the temperature increased, the surface acidity decreased since only the stronger acid sites were able to retain PY. Thus, the PY adsorption capacities at 573 K were taken as a measure of strong acid sites, while those at 373 K accounted for the total surface acidity (strong, medium, and weak acid sites).

TABLE 3

Surface Acidity versus Pyridine Adsorption and Apparent Rate Constants (k_a), Activation Parameters (E_a and ln A), and Selectivities to 1-Methylcyclopentene (σ) for Cyclohexene Skeletal Isomerization on $AlPO_4$, ZrO_2, and $AlPO_4$–ZrO_2 Catalysts

Catalyst	Pyridine (μmol m^{-2})		$k_a\,10^7$ (mol atm^{-1} s^{-1} m^{-2})	E_a (kcal mol^{-1})	ln A	σ
	373 K	573 K				
AP-0-873	1.3	0.03	0.02	13.8 ± 1.6	−3.9	1.2
APZr-5-873	1.5	0.05	0.15	14.6 ± 1.6	−2.7	1,2
APZr-7-873	2.2	0.06	0.39	8.9 ± 0.4	−5.4	1.4
APZr-10-873	2.3	0.07	0.51	8.7 ± 0.3	−5.1	1.5
APZr-25-873	1.6	0.17	1.62	10.0 ± 0.2	−2.4	2.4

It is evident from Table 3 that APZr catalysts exhibited not only an increased total acidity but also an increased density of strong acid sites (titrated at 573 K) compared with the AP-0-873 catalyst. The results in Table 3 also indicate that the density of strong acid sites increased with zirconia loading.

Catalytic Measurements

Model reactions were recommended as the best method for characterizing acidic industrial catalysts (54, 55). Thus, cyclohexene isomerization was one of the simplest reactions in studying stronger acid sites (Brønsted and Lewis) on solid catalysts (54–56). In the conversion of cyclohexene, there are various possibilities: (i) skeletal isomerization to methylcyclopentene isomers; (ii) hydrogen transfer reaction to cyclohexane and methylcyclopentane (55, 57, 58); and (iii) dehydrogenation to benzene (59). In this sense, Parmaliana *et al.* (57) indicated that cyclohexene can be considered a most reliable probe molecule for a number of catalytic functions: isomerization, hydrogen activation, and hydrogen transfer.

The results of this study indicate that cyclohexene conversion proceeds simply by skeletal isomerization (CSI) to 1- and 3-methylcyclopentene on all $AlPO_4$–ZrO_2 catalysts.

The cyclohexene conversion reaction data in all APZr catalysts were found to fulfill the Bassett–Habgood rate equation (60) for first-order reactions in which the partial reactant pressure is low and the adsorption rate is faster than the rate of surface reaction, the latter being the rate-determining step. In that sense, only the data below 20 mol% cyclohexene conversion (where the equilibrium reaction can be neglected) were used for the calculation. The Bassett–Habgood (60) equation was in the form

$$\ln[1/(1-X)] = k_a RT(W/F), \qquad [1]$$

where X is cyclohexene conversion, k_a apparent rate constant of the surface process, W catalyst weight, and F flow rate of carrier gas.

The $\ln[1/(1-X)]$ versus F^{-1} plots, according to Eq. [1], for the conversion of cyclohexene on APZr catalysts at various flow rates of the nitrogen carrier gas (30–60 $cm^3\ min^{-1}$) and different reaction temperatures are linear and also pass through the origin, indicating a good fit of the data to Eq. [1] and, so, the first-order process in the cyclohexene conversion. Also, the data for different catalyst particle sizes below 0.7 mm lie on the same plot; i.e., the reactions are not influenced by internal diffusion for catalyst particle sizes $\leq$0.7 mm. Furthermore, the catalytic runs have also been carried out at different weight ratios of catalyst from the cyclohexene introduced, showing that the fractional conversion of a pulse of reactant to products was independent of pressure, which determined the first-order reaction process. This behavior also ensured linear chromatography in the pulse mode, i.e., ensuring equilibrium chromatography.

Under the above experimental conditions apparent rate constants remained approximately constant after the first 15 pulses, when it decreased very slightly. Also, the selectivity to 1-MCPE remained almost unchanged with pulse number. Thus, APZr catalysts were difficult to deactivate by coke deposition, maintaining a relatively stable activity. In fact, the use of a microcatalytic pulse reactor also contributes to minimize the coke formation.

Table 3 gives, for all APZr catalysts, k_a (at a reaction temperature of 573 K) from linear plots of $\ln[1/(1-X)]$ versus W. Table 3 also includes activation parameters (E_a and $\ln A$), obtained from the Arrhenius equation by plotting $\ln k_a$ versus T^{-1}. The kinetic selectivity factors (σ) for CSI, obtained from the slope of $X_{1\text{-MCPE}}$-versus-$X_{3\text{-MCPE}}$ plots, are also included in Table 3.

The 98% confidence limits and the coefficient of determination (always over 0.99) for regressions were used to check the adequacy of the data. A Student t test of significance showed that these were significant at levels over 1%. At least three measurements were used to calculate each k_a value. All values were reproducible to within ca. 8%.

Table 3 shows that the introduction of small amounts of zirconia (5–25 wt%) into $AlPO_4$ produces catalysts that exhibit increased activity (at all $AlPO_4/ZrO_2$ weight ratios) in CSI as compared with $AlPO_4$, indicating an increase in surface acidity with zirconia loading. Thus, activity increases as zirconia content increases and, so, the catalytic activity of the APZr-25-873 catalyst is 84 times greater than that of AP-0-873. Moreover, the change in activity with the change in zirconia loading is similar to the change in surface density of strong acid sites also shown in Table 3. So, the catalytic activity of APZr catalysts correlates well with the acidity measured by gas chromatography through PY adsorption at 573 K.

Furthermore, with regard to the selectivity of the CSI reaction we have applied the Wheeler criterion (61) on the kinetic selectivity factor (σ) or first-order processes by plotting (Fig. 7) fractional conversion to 1-MCPE (X_1) versus that to 3-MCPE (X_3). We have also constructed optimum performance envelope (OPE) curves, which describe the selectivity behavior of products, by plotting X_1 and X_3 against total conversion (X_T) for different weight ratios of catalyst to cyclohexene (Fig. 7) for APZr-25-873 catalyst, such as described by Ko and Wojciechowski (62). We have plotted all the experimental data corresponding to different reaction temperatures and contact times on the same diagram. Using such a procedure, an insignificant scattering of the data was evident on the selectivity diagrams and so clear tendencies can be observed from these curves.

The results (straight lines at origin in all cases) show that 1- and 3-MCPE are stable primary competitive products from cyclohexene through a parallel process with first-order

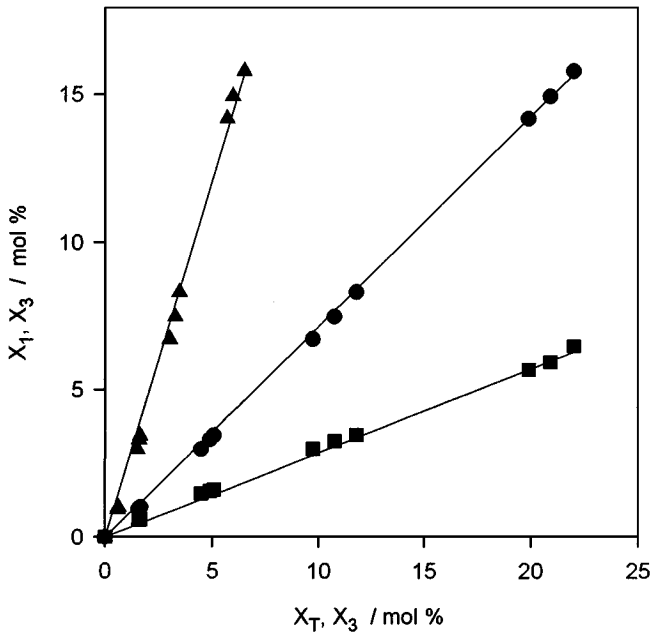

FIG. 7. OPE selectivity curves [(●) $X_{1\text{-MCPE}}$ (X_1) and (■) $X_{3\text{-MCPE}}$ (X_3) versus X_T] and Wheeler selectivities [σ; (▲) X_1 versus X_3] for cyclohexene skeletal isomerization on APZr-25-873 catalyst.

kinetics. They are formed at a constant rate in relation to feed conversion, and neither disappear nor accumulate due to secondary products. A primary product is defined as that produced from the reactant, no matter how many surface intermediates are involved in its formation. So, σ can be expressed by

$$\sigma = k_1/k_3 = X_1/X_3$$
$$= [A_1 \exp(-E_a/RT)]/[A_3 \exp(-E_a/RT)] = A_1/A_3,$$

since the σ selectivities (Table 3) were measured at different reaction temperatures and were found to be invariant with temperature (the apparent activation energies for 1- and 3-MCPE are quite similar for each catalyst), as expected for a mechanism involving a carbenium ion intermediate. Thus, as the preexponential factor is a function of stronger acid site number and these were different on each catalyst, the σ values are also different.

From Table 3, it is also evident that APZr-873 catalysts exhibit increased selectivity to 1-MCPE as compared with AP-0-873.

These results can be interpreted essentially as a consequence of the heterogeneity of acidic sites due to the fact that the catalytic reaction involves adsorbed species and the surface heterogeneity of the catalysts affects the activation energy for the reaction. Thus, the distribution of acid strength determines the energy barrier for the reaction to occur; the number of sites is also important. So, the global rate will be the sum of the individual rates on each type of site, each one proceeding with a different activation energy.

In this way, the differences in reaction rate originate in changes in the energies and number of reactive species. Moreover, the number of sites that are active for a given reaction depends mainly on the activation energy. Thus, strong acid sites are characterized by a lower activation energy while the relative abundance of such sites can be related to the relative activity.

Thus, the differences between the activities of APZr catalysts are due to differences in the number and strength of acid sites. The balance between (*i*) the amount of acid sites, which affects mainly the frequency factor values, and (*ii*) their activity, which affects mainly the activation energy, determines the sequence of catalytic activity in APZr catalysts.

So, the previously proposed mechanism for cyclohexene isomerization on $AlPO_4$ (63) can also be applied to APZr catalysts although the reaction intermediates ought to be of higher carbocationic character than $AlPO_4$. Thus, as Brönsted surface acidity increases, the more the carbocationic character of intermediates develops, the more the ratios of rates for 1- and 3-MCPE formation are expected to rise due to the higher stability of the 1-methylcyclopentyl carbenium ion (II) in relation to the 2-methylcyclopentyl carbenium ion (III) (64).

CONCLUSIONS

In summary, the incorporation of zirconia gel into $AlPO_4$ yielded $AlPO_4$–ZrO_2 materials that showed higher thermal stability and larger surface area as well as pore volume than pure components. Furthermore, they remained in the amorphous state at calcination temperatures up to 1073 K. Thermal treatment at 1273 K induced crystallization into the ZrO_2 tetragonal phase and into the $AlPO_4$- tridymite polymorph. Moreover, the transition from the tetragonal to the monoclinic phase did not take place. This higher thermal stability was responsible for its large surface area as well as pore volume in relation to pure components. SEM showed a nonhomogeneous distribution in morphology, texture, and particle size. Also, EDX and XPS indicated that the surface concentration ratios were practically the same as the expected values of stoichiometric composition. Moreover, ^{27}Al and ^{31}P MAS NMR showed that the local structure of the $AlPO_4$ support did not change with zirconia. Furthermore, the introduction of small amounts of zirconia (5–25 wt%) into $AlPO_4$ produced catalysts that exhibited improved catalytic activity for cyclohexene skeletal isomerization. The catalytic activity results can be well interpreted in terms of the differences in the number and strength of acid sites, gas chromatographically measured in terms of pyridine chemisorbed at 373 and 573 K. The results indicate that the density of strong acid sites, and hence catalytic activity, increased with zirconia loading.

ACKNOWLEDGMENTS

The authors acknowledge subsidies from the DGICYT (Project PB92/0816), Ministerio de Educacion y Cultura, and from the Consejeria de Educación y Ciencia (Junta de Andalucia), Spain. J. A. Navio thanks the Spanish MEC for financial support (Project PB96/1346). The authors also thank Dr. R. Ruiz (NMR Service, Universidad de Cordoba) for performing MAS NMR measurements. They also thank Professor M. Sullivan for linguistic revision of the manuscript.

REFERENCES

1. Bautista, F. M., Campelo, J. M., Garcia, A., Luna, D., Marinas J. M., and Romero, A. A., *Appl. Catal. A* **96**, 175 (1993), and references cited therein.
2. Cativiela, C., Fraile, J. M., Garcia, J. I., Mayoral, J. A., Campelo, J. M., Luna, D., and Marinas, J. M., *Tetrahedron Asymm.* **4**, 2507 (1993).
3. Campelo, J. M., Garcia, A., Herencia, J. F., Luna, D., Marinas, J. M., and Romero, A. A., *J. Catal.* **151**, 307 (1995).
4. Afxantidis, J., Bouchry, N., and Aune, J. P., *J. Mol. Catal. A* **102**, 49 (1995).
5. Bautista, F. M., Campelo, J. M., Garcia, A., Leon, J., Luna, D., and Marinas, J. M., *J. Chem. Soc. Perkin Trans.* **2**, 815 (1995).
6. Blanco, A., Campelo, J. M., Garcia, A., Luna, D., Marinas, J. M., and Romero, A. A., *J. Catal.* **137**, 51 (1992).
7. Bautista, F. M., Campelo, J. M., Garcia, A., Luna, D., Marinas, J. M., Romero, A. A., Navio, J. A., and Macias, M., *J. Catal.* **145**, 107 (1994).
8. Campelo, J. M., Garcia, A., Luna, D., Marinas, J. M., Romero, A. A., Navio, J. A., and Macias, M., *J. Chem. Soc. Faraday Trans.* **90**, 2265 (1994).
9. Lindblad, T., Rebenstorf, B., Yan, Z. G., and Andersson, S. L. T., *Appl. Catal. A* **112**, 87 (1994).
10. Andersson, S. L. T., *Appl. Catal. A* **112**, 209 (1994).
11. Kuo, P. S., and Yang, B. L., *J. Catal.* **117**, 301 (1989).
12. Lakshmi, L. J., and Rao, P. K., *Catal. Lett.* **21**, 345 (1993).
13. Lakshmi, L. J., and Rao, P. K., Mastikhin, V. M., and Nosov, A. V., *J. Phys. Chem.* **97**, 11373 (1993).
14. Campelo, J. M., Chakraborty, R., and Marinas, J. M., *Syn. Commum.* **26**, 415 (1996).
15. Campelo, J. M., Chakraborty, R., and Marinas, J. M., *Syn. Commum.* **26**, 1639 (1996).
16. Tanabe, K., *Mater. Chem. Phys.* **13**, 347 (1985).
17. Chokkaram, S., Srinivasan, R., Milburn, D., and Davis, B. H., *J. Colloid Interface Sci.* **164**, 160 (1994), and references cited therein.
18. Srinivasan, R., and Davis, B. H., *Catal. Lett.* **14**, 165 (1992).
19. Srinivasan, R., Harris, M. B., Simpson, S. F., De Angelis, R. J., and Davis, B. H., *J. Mater. Res.* **3**, 787 (1988), and references cited therein.
20. Tichit, D., El Alami, D., and Figueras, F., *Appl. Catal. A* **145**, 195 (1996).
21. Mercera, P. D. L., van Ommen, J. G., Doesburg, E. B. M., Burggraaf, A. J., and Ross, J. R. H., *Appl. Catal.* **78**, 79 (1991), and references cited therein.
22. Duchet, J. C., Tilliette, M. J., and Cornet, D., *Catal. Today* **10**, 507 (1991).
23. Arata, K., *Adv. Catal.* **37**, 165 (1990), and references cited therein.
24. Miller, J. B., Rankin, S. E., and Ko, E. I., *J. Catal.* **148**, 673 (1994).
25. Corma, A., Fornes, V., Juan Rajadell, M. I., and Lopez-Nieto, J. M., *Appl. Catal. A* **116**, 151 (1994).
26. Huang, Y. Y., McCarthy, T. J., and Sachtler, W. M. H., *Appl. Catal.* **148**, 135 (1996).
27. Hino, M., Kabayashi, S., and Arata, K., *J. Am. Chem. Soc.* **101**, 139 (1979).
28. Comelli, R. A., Vera, C. R., and Parera, J. M., *J. Catal.* **151**, 96 (1995).
29. Ward, D. A., and Ko, E. I., *J. Catal.* **157**, 321 (1995).
30. Campelo, J. M., Marinas, J. M., Mendioroz, S., and Pajares, J. A., *J. Catal.* **101**, 484 (1986).
31. Barrett, E. P., Joyner, L. S., and Halenda, P., *J. Am. Chem. Soc.* **73**, 373 (1951).
32. Halsey, G., *J. Chem. Phys.* **16**, 931 (1948).
33. Campelo, J. M., Garcia, A., Luna, D., and Marinas J. M., *J. Mater. Sci.* **25**, 2513 (1990).
34. Keramidas, V., and White, W. B., *J. Am. Ceram. Soc.* **57**, 22 (1974), and references cited therein.
35. Mercera, P. D. L., van Ommen, J. G., Doesburg, E. B. M., Burggraaf, A. J., and Ross, J. R. H., *Appl. Catal.* **57**, 127 (1990).
36. Navio, J. A., Colon, G., Sanchez-Soto, P. J., and Macias, M., *Chem. Mater.* **9**, 1256 (1997).
37. Cornell, R. M., and Giovanoli, R., *J. Chem. Soc. Chem. Commun.*, 413 (1987).
38. Parida, K. M., and Pattnayak, P. K., *J. Colloid Interface Sci.* **182**, 381 (1996).
39. Zhao, B. Y., Xu, X. P., Ma, H. R., Gao, J. M., Sun, D. H., Wang, R. Q., and Tang, Y. Q., *Acta Phys. Chin. Sin.* **9**, 8 (1983).
40. Srinivasan, R., Watkins, T. R., Hubbard, C. R., and Davis, B. H., *Chem. Mater.* **7**, 725 (1995).
41. Livage, J., Doi, K., and Mazieres, C., *J. Am. Ceram. Soc.* **51**, 349 (1967).
42. Ishigame, M., and Sakurai, T., *J. Am. Ceram. Soc.* **60**, 367 (1977).
43. Teufer, G., *Acta Crystallogr.* **12**, 507 (1959).
44. Schild, Ch., Wokaum, A., Köppel, R. A., and Baiker, A., *J. Catal.* **130**, 657 (1991).
45. Voronko, Y. K., Ignatev, B. V., Lomonova, E. E., Osiko, V. V., and Sobol, A. A., *Soviet Phys. Solid State* **22**, 603 (1980).
46. Arashi, H., and Ishigame, M., *Phys. Status Solidi* **71**, 313 (1982).
47. Muller, D., Jahn, E., Ladwig, G., and Haubenreisser, U., *Chem. Phys. Lett.* **109**, 332 (1984).
48. Blackwell, C. S., and Paton, R. L., *J. Phys. Chem.* **88**, 6135 (1984).
49. Brunauer, S., Deming, L. S., Deming, W. S., and Teller, E., *J. Am. Chem. Soc.* **62**, 1723 (1940).
50. Sing, K. S. W., Everett, D. H., Haul, R. A. W., Moscou, L., Pierotti, R. A., Rouquerol, J., and Siemieniewska, T., *Pure Appl. Chem.* **57**, 603 (1985).
51. Harkins, W. D., and Jura, G., *J. Chem. Phys.* **11**, 431 (1943).
52. Broekhoff, J. C. P., and Linsen, B. G., *in* "Physical and Chemical Aspects of Adsorbents and Catalysts" (B. G. Linsen, Ed.), pp. 1–62. Academic Press, London, 1970.
53. Mata Arjona, A., Parra Soto, J. B., and Otero Arean, C., *Stud. Surf. Sci. Catal.* **10**, 175 (1982).
54. Kijenski, J., and Baiker, A., *Catal. Today* **5**, 1 (1989).
55. Guisnet, M., *Acc. Chem. Res.* **23**, 392 (1990).
56. Bourdillon, G., Gueguen, C., and Guisnet, M., *Appl. Catal.* **61**, 123 (1990).
57. Parmaliana, A., Iannibello, A., Frusteri, F., Tsiakaras, T., and Giordano, N., *in* "Catalysis 1987" (J. W. Ward, Ed.), p. 43. Elsevier, Amsterdam, 1988.
58. Dwyer, J., Karim, K., and Ojo, A. F., *J. Chem. Soc. Faraday Trans.* **87**, 783 (1991).
59. Campelo, J. M., Climent, M. S., Garcia, A., Luna, D., Marinas J. M., Romero, A. A., Navio, J. A., and Macias, M., *J. Mater. Chem.* **5**, 2019 (1995).
60. Bassett, D., and Habgood, H. W., *J. Phys. Chem.* **64**, 769 (1960).
61. Wheeler, A., *Adv. Catal.* **3**, 529 (1951).
62. Ko, A. N., and Wojciechowski, B. W., *Prog. React. Kinet.* **12**, 201 (1983).
63. Campelo, J. M., Garcia, A., Luna, D., and Marinas, J. M., *J. Catal.* **111**, 106 (1988).
64. Viruela-Martin, P. M., Nebot, I., Viruela-Martin, R., and Planelles, J., *J. Chem. Soc. Perkin Trans.* **2**, 49 (1986).